A comparison of a model using the FORMOSAT-3/COSMIC data with the IRI model

Yoshihiro Kakinami[1*], Jann-Yenq Liu[1,2], and Lung-Chih Tsai[2]

[1]*Institute of Space Science, National Central University, No. 300 Jhongda Rd. Jhongli, Taoyuan 32001, Taiwan*
[2]*Center for Space and Remote Sensing Research, National Central University, No. 300 Jhongda Rd. Jhongli, Taoyuan 32001, Taiwan*

In this study, an empirical model constructed using data of FORMOSAT3/COSMIC (F3/C) from 29 June, 2006, to 17 October, 2009, retrieves altitude profiles of electron density (N_e). The model derives global N_e profiles from 150 to 590 km altitude as functions of the solar EUV flux, day of year, local time and location under geomagnetically quiet conditions ($K_p < 4$). N_e profiles derived by the model are further compared with those of the International Reference Ionosphere (IRI). Results show that the F_2 peak altitude h_mF_2 and the electron density N_mF_2, as well as the electron density above, derived by the model are lower than those of the IRI model. The F3/C model reproduces observations of F3/C well at 410-km altitude while the IRI model overestimates them. The overestimation of the IRI model becomes large with decrease of EUV flux. It is found that the topside vertical scale height of the F3/C model shows high values not only magnetic dip equator but also middle latitude. The results differ significantly from those of IRI, but agree with those observed by topside sounders, Alouette and ISIS satellites.
Key words: IRI, electron density, topside ionosphere, empirical model, FORMOSAT-3/COSMIC, vertical scale height.

1. Introduction

The International Reference Ionosphere (IRI) has been developed since 1978 (Rawer *et al.*, 1978) and is established as the most standard and reliable ionospheric empirical model. Since a large amount of ionosonde data has been used, IRI derives a relatively accurate electron density (N_e) profile below the F_2 peak. However, the IRI model might still have some shortcomings in the topside ionosphere, because very limited satellite data are included. Bilitza (2004) and Bilitza *et al.* (2006) based on Alouette/ISIS topside sounder observations reported that the IRI model overestimates N_e above the F_2 peak height. Furthermore, Kakinami *et al.* (2008) found an in-situ N_e observation at a 600-km altitude with the Hinotori satellite which differed from the IRI N_e. This shortcoming also results in a difference between the Total Electron Content (TEC) reproduction and real observations, because the TEC is calculated using an integration of the N_e profile. Meanwhile, the IRI model overestimates the TEC in the equatorial region (Bilitza and Williamson, 2000) during high solar activity, while the IRI model overestimates and underestimates the TEC over Taiwan (24°N 120°E) during low and high solar activity, respectively (Kakinami *et al.*, 2009).

Six FORMOSAT-3/COSMIC (F3/C) micro satellites which constituted a global positioning system (GPS) occultation experiment (GOX) payload were launched on 14 April, 2006, and put into a low Earth orbit of 800-km altitude with a 72° inclination. An average of 1800 electron density profiles was obtained in a day globally. Lei *et al.* (2007) reported that N_e profiles measured with F3/C are consistent with N_mF_2 and h_mF_2 obtained with incoherent scatter radars at Millstone Hill and Jicamarca. An N_e profile obtained using GOX has an advantage in its coverage of observations, compared with the peak density and peak altitude of the ionosphere obtained with ground-based observations, because it was able to cover ocean and desert areas, where there are usually no receivers. Taking advantage of this feature, we have constructed an empirical model of the N_e profile measured with F3/C, which reproduces the N_e profile globally. In this paper, we describe the methodology in constructing the model and compare the empirical model based on F3/C observations with the IRI model.

2. Methodology of the Construction of an Empirical Model

The methodology of constructing an empirical model based on F3/C data is described in this section. Henceforth, the empirical model based on N_e profiles obtained by F3/C is referred to as the F3/C model. The F3/C model reproduces N_e as functions of the solar EUV flux, day of year (DOY), local time (LT), altitude and location. A similar methodology has been applied to empirical models of transition height (Marinov *et al.*, 2004; Kutiev and Marinov, 2007), vertical scale height in the top-

side ionosphere (Kutiev *et al.*, 2006) and TEC over Taiwan (Kakinami *et al.*, 2009). Daily EUV (0.1–50 nm) measured by the Solar Heliospheric Observatory (SOHO) (Judge *et al.*, 1998) and posted on the web site of the Space Science Center of the University of Southern California (http://www.usc.edu/dept/space_science/), is used to construct the model. The released EUV fluxes are modified using the Sun-Earth distance because the released daily EUV fluxes are adjusted at 1 AU. Data are not used in the model construction when the EUV exceeds 10^{11} photon/cm^2 sec due to a solar flare. The EUV variation used in the F3/C model, which is excluded the fluctuated day, is shown in Fig. 1. Observed N_e profiles are accumulated under geomagnetically quiet conditions ($K_p < 4$) from 29 June, 2006, to 17 October, 2009. Since N_e profiles are calculated using the Abel inversion with an assumption of spherical symmetry, the errors mainly appear below 250 km around the equatorial ionization anomaly region (Liu *et al.*, 2010), which leads to a negative value of the N_e profile in some cases. Therefore, observed N_e profiles showing a negative value are not used in the model construction. At first, the empirical model which has functions of EUV, DOY and LT is constructed in each 3-dimensional bin whose size is 30° in longitude, 18° in latitude and 20 km (40 km) altitude between 150 and 390 (390 and 590) km altitude with steps of 10° in longitude and 6° in latitude. It is assumed that the solar flux variation of $\log_{10}(N_e)$ is proportional to the EUV flux, while the DOY and LT variation of $\log_{10}(N_e)$ are derived using a combination of trigonometric functions of wavenumbers 1–3 and 1–4, respectively. The modeled functions are calculated for each bin. The functions for F, DOY and LT are defined as follows:

$$f(\text{EUV}) = a_1 + a_2 \text{EUV}, \tag{1}$$

$$
\begin{aligned}
g(\text{DOY}) &= b_1 + \sum_{i=1}^{3} (b_{2i} \cos 2\pi i \cdot \text{DOY} \\
&\quad + b_{2i+1} \sin 2\pi i \cdot \text{DOY}) \\
&= b_1 g_1' + \cdots + b_7 g_7', \tag{2}
\end{aligned}
$$

$$
\begin{aligned}
h(\text{LT}) &= c_1 + \sum_{i=1}^{4} \left(c_{2i} \cos \frac{\pi i \cdot \text{LT}}{12} + c_{2i+1} \sin \frac{\pi i \cdot \text{LT}}{12} \right) \\
&= c_1 h_1' + \cdots + c_9 h_9', \tag{3}
\end{aligned}
$$

where a, b, c are coefficients for fitting. DOY is normalized by the length of the year. The function reproducing N_e is assumed to be the product of these 3 functions. Then we can obtain:

$$
\begin{aligned}
\log_{10} N_e(\text{EUV, DOY, LT}) &= f(\text{EUV}) \cdot g(\text{DOY}) \cdot h(\text{LT}) \\
&= \sum_{i,j,k} a_i f_i' \cdot b_j g_j' \cdot c_k h_k' \\
&= \sum_{n=1}^{126} \alpha_n \log_{10} N_{e_n}', \tag{4}
\end{aligned}
$$

where $n = (i-1) \times 63 + (j-1) \times 9 + k$, $i = 1, 2$, $j = 1, \ldots, 7$, $k = 1, \ldots, 9$. In order to calculate the coefficients α, more than 126 data are required. The α can be obtained by solving the following normal-equation
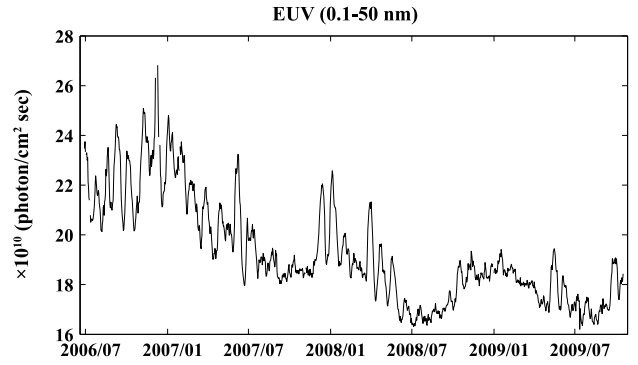

Fig. 1. EUV variation observed with SOHO from 29 June, 2006, to 17 October, 2009. Only data used in the construction of the F3/C model are shown.
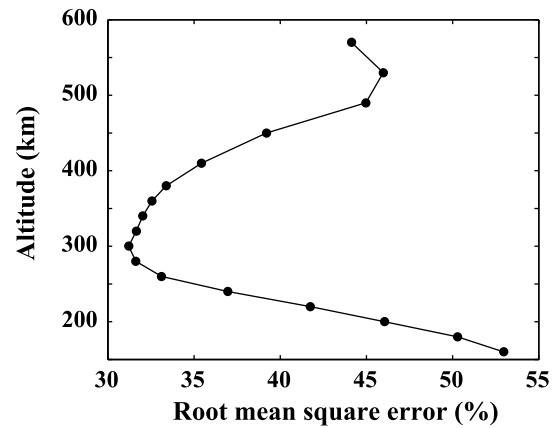

Fig. 2. Variation of root mean square error of the F3/C model with altitude.

matrix:

$$
\begin{pmatrix}
\sum \log_{10} N_e \cdot \log_{10} N_{e_1}' \\
\vdots \\
\sum \log_{10} N_e \cdot \log_{10} N_{e_{126}}'
\end{pmatrix}
= \begin{pmatrix}
\sum \log_{10} N_{e_1}' \cdot \log_{10} N_{e_1}' & \cdots & \sum \log_{10} N_{e_1}' \cdot \log_{10} N_{e_{126}}' \\
\vdots & \ddots & \vdots \\
\sum \log_{10} N_{e_{126}}' \cdot \log_{10} N_{e_1}' & \cdots & \sum \log_{10} N_{e_{126}}' \cdot \log_{10} N_{e_{126}}'
\end{pmatrix}
\begin{pmatrix}
\alpha_1 \\
\vdots \\
\alpha_{126}
\end{pmatrix}. \tag{5}
$$

The α are calculated in each 3-dimensional bin. Finally, the modeled N_e is obtained by linearly interpolating between the bins.

3. Results and Discussion

In order to estimate the accuracy of the F3/C model, the root-mean-square error (RMS) is calculated as follows,

$$\text{RMS} = \sqrt{\frac{1}{n} \sum_{i=1}^{n} \{(o_i - m_i)/m_i\}^2}, \tag{6}$$

where n, o_i, m_i, denote the data number, the N_e observed with F3/C, and the N_e derived by the F3/C model, respectively. RMSs at each altitude level are displayed in Fig. 2. The RMS is over 50% below 200 km while the RMS decreases with increasing altitude, and shows a minimum
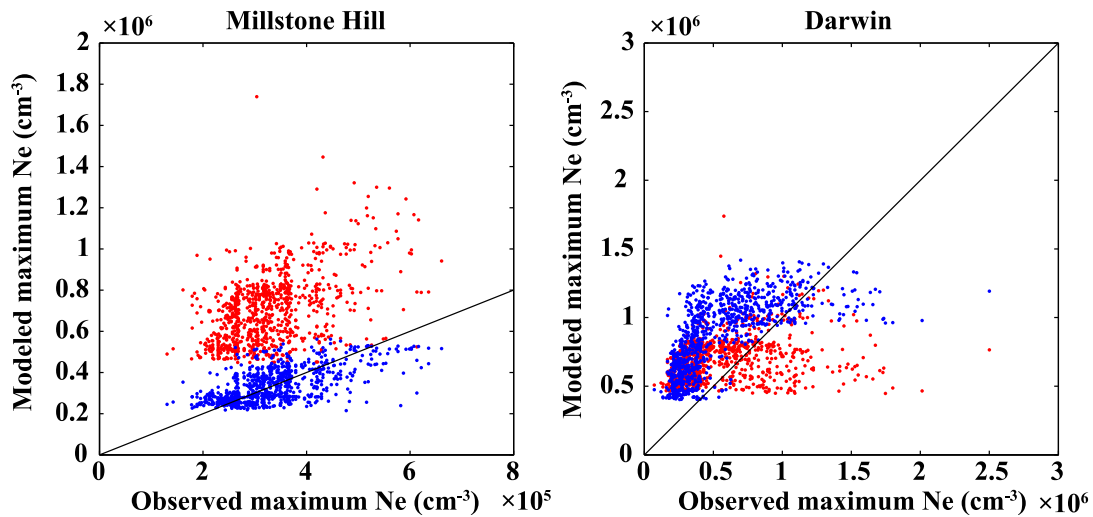
Fig. 3. Comparison of peak electron density derived by the F3/C model and the IRI model with ionosonde observations at 1200 LT at Millstone Hill (left) and Darwin (right) from 29 June, 2006, to 17 October, 2009. Red and blue dots indicate the F3/C and the IRI model results.
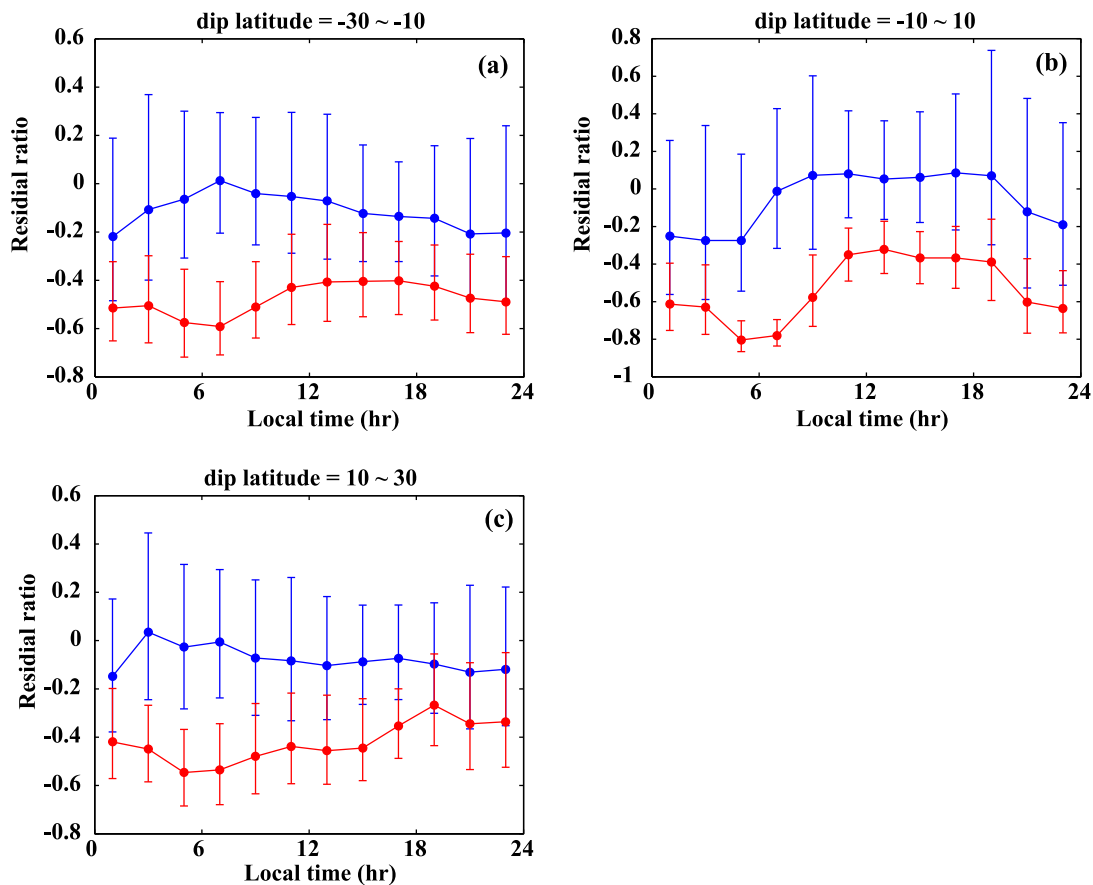

Fig. 4. Local time variation of the residual ratios for the F3/C (blue) and IRI (red) models in (a) dip latitude $= -30 \sim -10$, (b) dip latitude $= -10 \sim 10$ and (c) dip latitude $= 10 \sim 30$. Dots and error bars denote median and quartiles.

value at 300 km. The RMS increases with increasing altitude over 300 km and reaches about 45% around 500 km. Below 250 km, the estimation error of the N_e profile is very large due to the fundamental issue of the Abel inversion (Liu *et al.*, 2010), and the data used in the construction have inherent errors. Such errors might produce a high dispersion and show high RMS. On the other hand, since a similar high variability is seen in the N_e model using the

HINOTORI data at 600 km (Kakinami *et al.*, 2008), the dispersion of N_e might be high above 400 km.

The peak N_e calculated with the F3/C model are compared with those measured with ionospondes (Millstone Hill at 71.5°W, 42.6°N and Darwin at 131.0°E, 12.7°S) and IRI2007 with standard options (henceforth, we use the same IRI version) from 29 June, 2006, to 17 October, 2009, under geomagnetically quiet conditions, $K_p < 4$ (Fig. 3). The
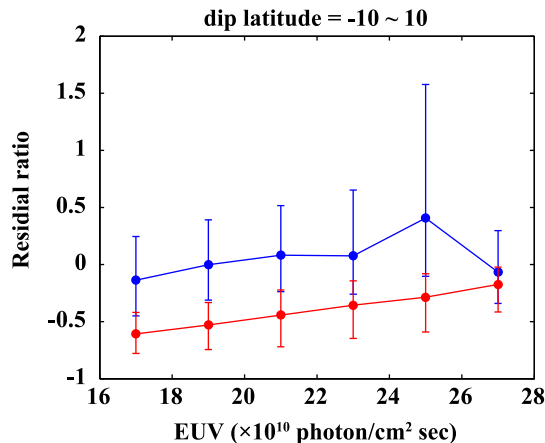
Fig. 5. Solar flux variation of the residual ratios for the F3/C (blue) and IRI models (red) in dip latitude $= -10 \sim 10$. Dots and error bars denote median and quartiles.
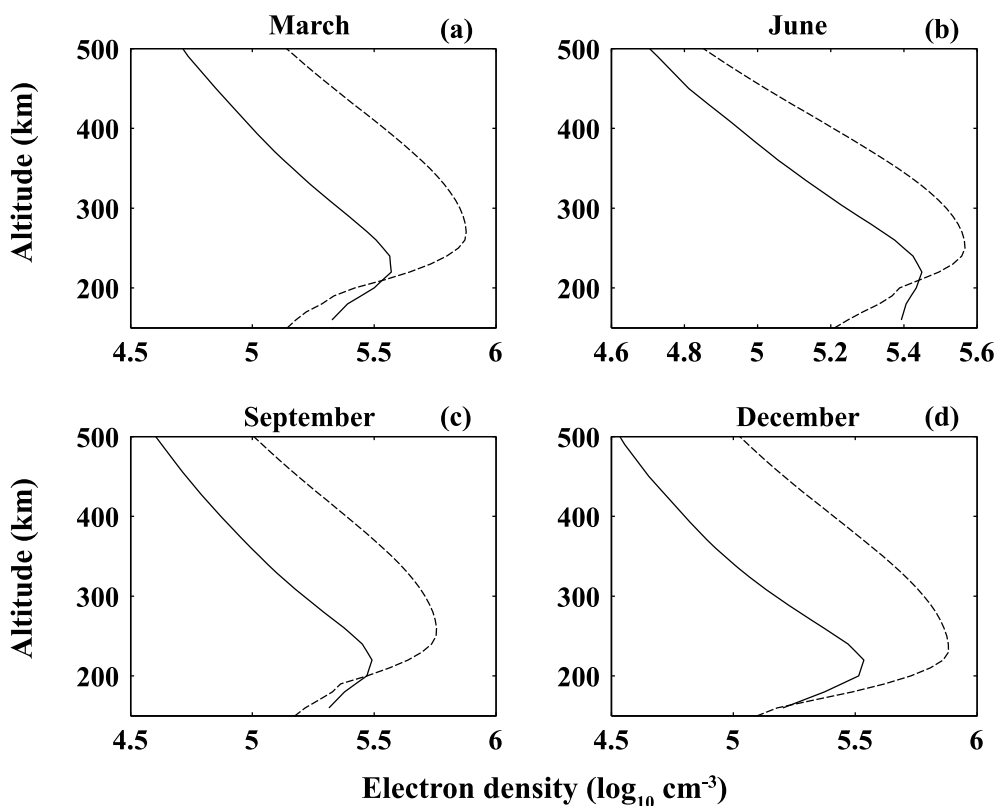

Fig. 6. Electron density profiles derived by the F3/C (solid line) and IRI models (dashed line) at 42.5°N 288.5°E at 1200 LT in March (a), June (b), September (c) and December (d). Intensities of EUV applied to calculations are 1.99, 1.99, 1.84 and 2.20×10^{11} photon/cm^2 sec, which are the actual conditions of solar flux in each month of 2007.

results with IRI match the observations at Millstone Hill, while those with the F3/C model overestimate the observations. Meanwhile, both models overestimate at Darwin in many cases. This result indicates that the reproduction of peak density by the IRI also has shortcomings at some locations.

In order to compare the observed N_e using F3/C with the F3/C and IRI model, residual ratios, $(o_i - m_i)/m_i$, where o_i and m_i denote the observed N_e at 410 km and the modeled N_e at 410 km, are calculated. Figure 4 displays the local time variation of the residual ratios for the F3/C and IRI models. Though the F3/C model slightly overes-

timates the observations by 10–20% during night time in all latitudes, the F3/C model agrees with the observations on the whole. However, the IRI model always overestimates observations by 40–60% at all local times and latitudes. Figure 5 shows the solar flux variation of the residual ratios for the F3/C and IRI models. The F3/C model shows a good agreement with the observations except for EUV $> 24 \times 10^{10}$ photon/cm^2 sec. As shown in Fig. 1, since the data number for EUV $> 24 \times 10^{10}$ photon/cm^2 sec is very small, the reliability of the F3/C model is less than that for EUV $< 24 \times 10^{10}$ photon/cm^2 sec. On the other hand, the IRI model overestimates the observations
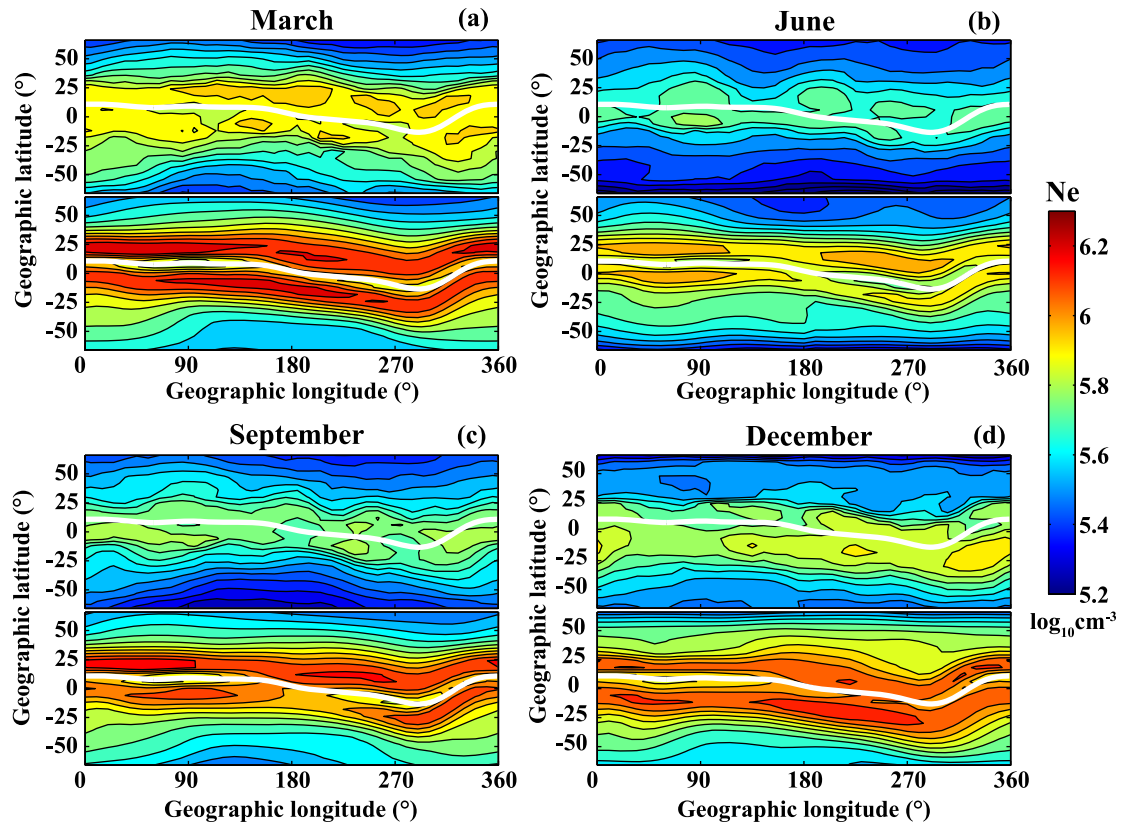
Fig. 7. Peak electron density maps derived by F3/C (top) and IRI model (bottom) at 1200 LT in March (a), June (b), September (c) and December (d). White curves indicate magnetic equator. Intensities of EUV applied to calculations are the same as Fig. 6.
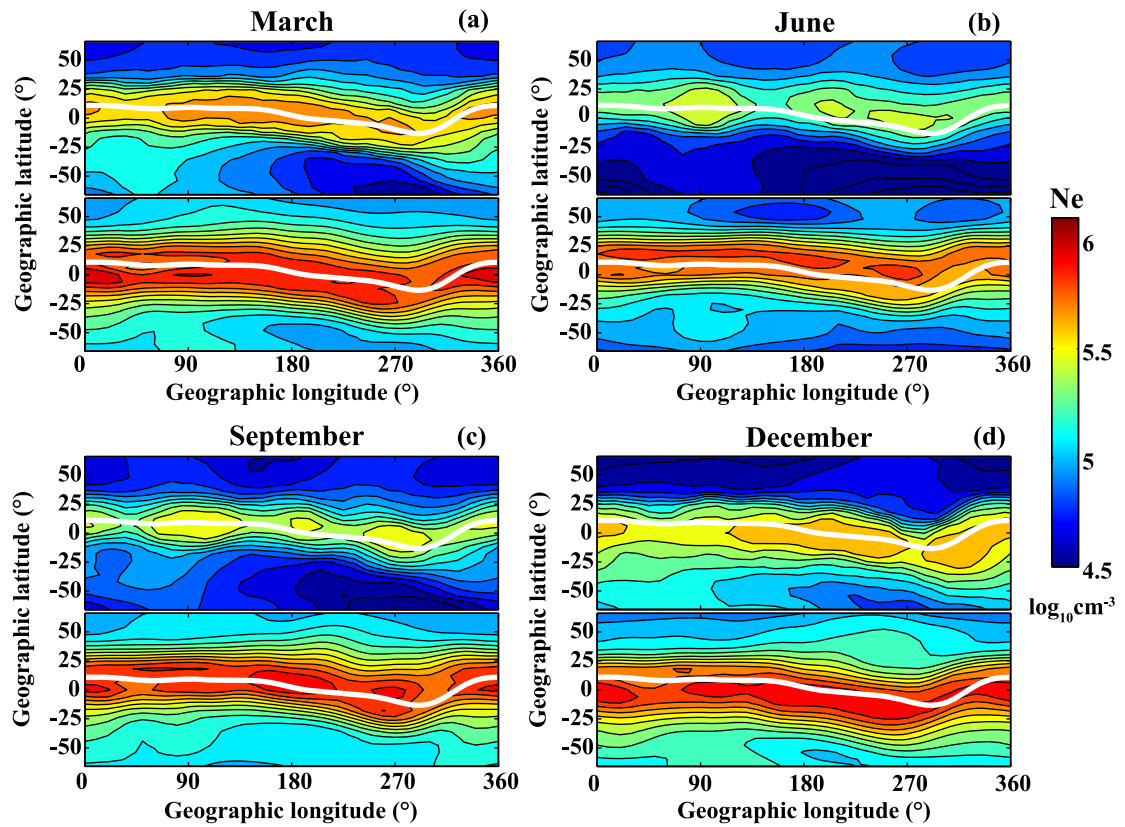

Fig. 8. Electro density maps at 450 km derived by F3/C (top) and IRI model (bottom) at 1200 LT in March (a), June (b), September (c) and December (d). White curves indicate magnetic equator. Intensities of EUV applied to calculations are the same as Fig. 6.
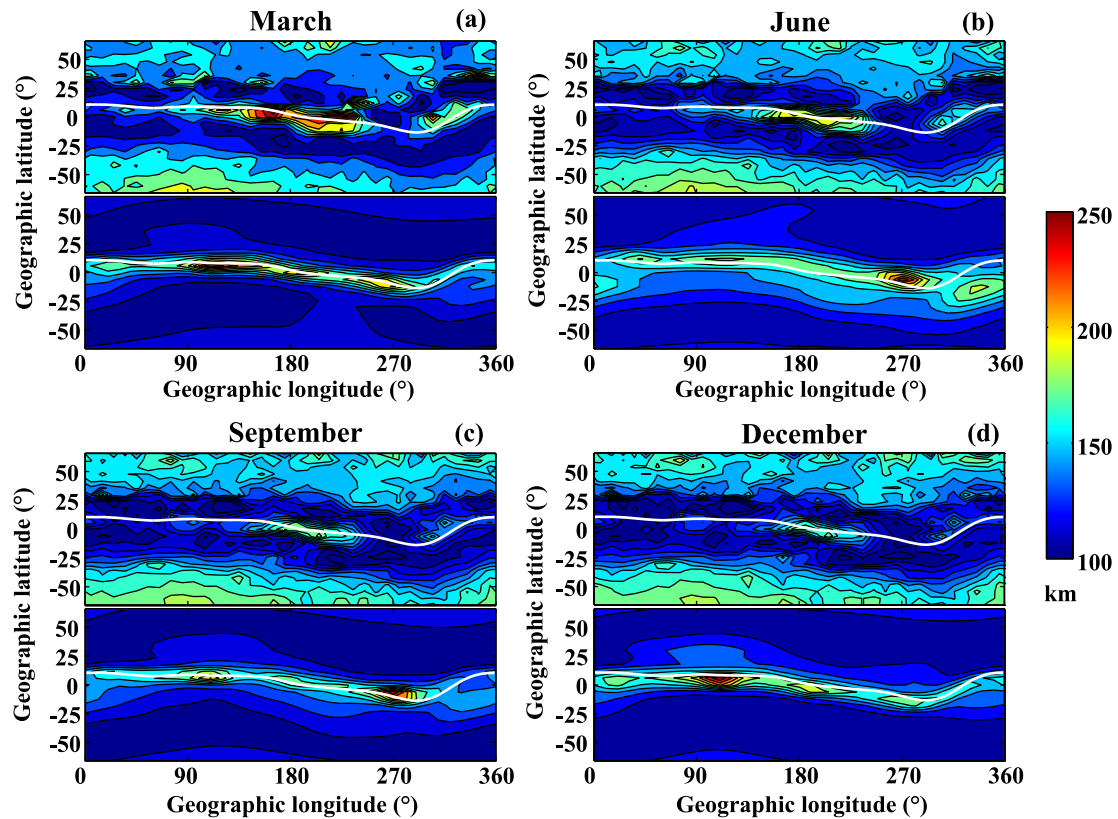
Fig. 9. Vertical scale height at 450 km derived by the F3/C model (top) and IRI model (bottom) at 1200 LT in March (a), June (b), September (c) and December (d). White curves indicate magnetic equator. Intensities of EUV applied in the calculations are the same as Fig. 6.

when EUV is low. The accuracy of the IRI model improves with an increase of EUV. This tendency of the IRI model to solar flux is similar to that of TEC over Taiwan (Kakinami *et al.*, 2009).

The altitude profile of N_e derived by the F3/C and the IRI models above Inamori Hall, Kagoshima University (42.5°N 288.5°E), where the IRI 2009 workshop was held, are shown in Fig. 6. The N_e derived by the IRI model is higher than that of the F3/C model at, and above the peak height in all seasons as shown in Figs. 4 and 5. In addition, the peak altitude h_mF_2 derived by the IRI model is higher than that of the F3/C model in all seasons. The vertical scale height (VSH) of the IRI model, which is defined as $-dh/d(\ln N_e)$ (Kutiev *et al.*, 2006), is slightly lower than that of the F3/C model in June. The N_e derived by IRI is lower than that of the F3/C model in the lower ionosphere in all seasons except December.

Figure 7 shows the seasonal variation of peak N_e (N_mF_2) at 1200 LT derived by the F3/C (top panel) and the IRI (bottom panel) models. The maximum of N_mF_2 is located beside the magnetic equator for both models. N_mF_2 derived by IRI is higher than that of the F3/C model in all seasons. A longitudinal structure of N_mF_2 exists in both models. Small patch-like maxima of N_mF_2 appear in the F3/C model, while wide-longitude-range maxima of N_mF_2 appear in IRI in March (Fig. 7(a)). A four-peak (2-peak) longitudinal structure is detected in the F3/C (IRI) model in June. The IRI model shows a clear 2-peak longitudinal structure in September. On the other hand, the F3/C model displays a 2-peak or more small-scale longitudinal structure

in September. A four or three-peak structure appears in both models in December.

The seasonal variation of N_e at 450 km derived by the F3/C and IRI models are shown in Fig. 8. The N_e derived by the IRI model is generally higher than that of the F3/C model around the magnetic equator. In contrast to the N_mF_2 shown in Fig. 7, a large-scale longitudinal structure, which is similarly reported by many scientists (e.g. Sagawa *et al.*, 2005; Immel *et al.*, 2006; Lin *et al.*, 2007; Kakinami *et al.*, 2011), is clearly seen around the magnetic equator in the F3/C model. According to Kakinami *et al.* (2011), the 4-peak structure of N_e at 660 km observed with the DEMETER satellite is the most pronounced in September while a 3-peak structure appears in March and December. Though the IRI model also shows a longitudinal structure, the longitudinal structure retrieved with the F3/C model is more pronounced than that of the IRI and its seasonal variation agrees with previous studies.

Seasonal variations of VSH at 450 km derived by the F3/C and IRI models are shown in Fig. 9. The IRI model shows a maxima of VSH along the magnetic equator with a 10° latitude width while the F3/C model only displays a small maxima of VSH around 140–240°E and 300°E near the magnetic equator. In the F3/C model, maxima of VSH around 140–240°E near the magnetic equator are always significant in all seasons, which show a maximum value in March. However, a maximum of VSH around 300°E is only significant in March. The longitudinal structure seen in the VSH derived by the F3/C model differs from those of N_e at 450 km (Fig. 8). Meanwhile, 3 or 4 maxima of VSH

derived by the IRI model appear around the magnetic equator. The location of each peak roughly corresponds to the locations of the maximum of N_e shown in Fig. 8. A significant difference in the VSH between the F3/C and the IRI models appears in the middle latitude. The VSH derived by the IRI model only shows a maximum around the magnetic equator, a sharp drop away from the magnetic equator and is almost constant in low and middle latitudes. Meanwhile, VSH derived by the F3/C model shows maxima (minima) around magnetic equator (beside geomagnetic equator) and increases with increasing latitude in low and middle latitudes. Similar VSH results are observed not only in F3/C data (Liu *et al.*, 2008) but also by the topside sounder onboard the Alouette and ISIS satellites (Kutiev and Marinov, 2007). Especially, VHS derived by the F3/C model higher than 50°S is higher than the magnetic equator in September and December.

4. Summary

We have constructed an empirical model based on N_e profiles observed with F3/C under geomagnetically quiet conditions ($K_p < 4$). The F3/C model derives global N_e profiles between altitudes of 150 and 590 km as functions of the solar EUV flux, day of year, local time and location. The N_e above the F_2 peak, and the F_2 peak altitude, derived by the F3/C model is lower than those derived by the IRI. The F3/C model reproduces a longitudinal structure better than the IRI model. The F3/C model also derives VSH which show good agreement with measurements obtained from topside sounders onboard the Alouette and ISIS satellites. Since the F3/C model has a big advantage of greater data coverage, it helps us to understand a variety of upper ionospheric phenomenon. As a result, the F3/C model contributes an improvement over the IRI model.

References

Bilitza, D., A correction for the IRI topside electron density model based on Alouette/ISIS topside sounder data, *Adv. Space Res.*, **33**, 838–843, 2004.

Bilitza, D. and R. Williamson, Towards a better representation of the IRI topside based on ISIS and Alouette data, *Adv. Space Res.*, **25**(1), 149–152, 2000.

Bilitza, D., B. W. Reinsch, S. Radicella, S. Pulinets, T. Gulyaeva, and L. Triskova, Improvements of the international reference ionosphere

model for the topside electron density profile, *Radio Sci.*, **41**, RS5S15, doi:10.1029/2005RS003370, 2006.

Immel, T. J., E. Sagawa, S. L. England, S. B. Henderson, M. E. Hagan, S. B. Mende, H. U. Frey, C. M. Swenson, and L. J. Paxton, Control of equatorial ionospheric morphology by atmospheric tides, *Geophys. Res. Lett.*, **33**, L15108, doi:10.1029/2006GL026161, 2006.

Judge, D. L., D. R. McMullin, S. Ogawa, D. Hovestadt, B. Klecker, M. Hilchenbach, L. R. Canfield, R. E. Vest, R. Watts, C. Tarrio, M. Kuhne, and P. Wurz, First solar EUV irradiances obtained from SOHO by the CELIAS/SEM, *Sol. Phys.*, **177**, 161–173, 1998.

Kakinami, Y., S. Watanabe, and K.-I. Oyama, An empirical model of electron density in low latitude at 600 km obtained by Hinotori satellite, *Adv. Space Res.*, **41**, 1494–1498, doi:10.1016/j.asr.2007.09.031, 2008.

Kakinami, Y., C. H. Chen, J. Y. Liu, K.-I. Oyama, W. H. Yang, and S. Abe, Empirical models of Total Electron Content based on functional fitting over Taiwan during geomagnetic quiet condition, *Ann. Geophys.*, **27**, 3321–3333, 2009.

Kakinami, Y., C. H. Lin, J. Y. Liu, M. Kamogawa, S. Watanabe, and M. Parrot, Daytime longitudinal structure of electron density and temperature in the topside ionosphere observed by the Hinotori and DEMETER satellites, *J. Geophys. Res.*, doi:10.1029/2010JA015632, 2011.

Kutiev, I. and P. Marinov, Topside sounder model of scale height and transition height characteristics of the ionosphere, *Adv. Space Res.*, **39**, 759–766, 2007.

Kutiev, I., P. Marinov, and S. Watanabe, Model of topside ionosphere scale height based on topside sounder data, *Adv. Space Res.*, **37**, 943–950, 2006.

Lei, J., S. Syndergaard, A. G. Burns, S. C. Solomon, W. Wang, Z. Zeng, R. G. Roble, Q. Wu, Y.-H. Kuo, J. M. Holt, S.-R. Zhang, D. L. Hysell, F. S. Rodrigues, and C. H. Lin, Comparison of COSMIC ionospheric measurements with ground-based observations and model predictions: Preliminary results, *J. Geophys. Res.*, **112**, A07308, doi:10.1029/2006JA012240, 2007.

Lin, C. H., W. Wang, M. E. Hagan, C. C. Hsiao, T. J. Immel, M. L. Hsu, J. Y. Liu, L. J. Paxton, T. W. Fang, and C. H. Liu, Plausible effect of atmospheric tides on the equatorial ionosphere observed by the FORMOSAT-3/COSMIC: Three-dimensional electron density structures, *Geophys. Res. Lett.*, **34**, L11112, doi:10.1029/2007GL029265, 2007.

Liu, L., M. He, W. Wan, and M.-L. Zhang, Topside ionospheric scale heights retrieved from Constellation Observing System for Meteorology, Ionosphere, and Climate radio occultation measurements, *J. Geophys. Res.*, **113**, A10304, doi:10.1029/2008JA013490, 2008.

Liu, J. Y., C. Y. Lin, C. H. Lin, H. F. Tsai, S. C. Solomon, Y. Y. Sun, I. T. Lee, W. S. Schreiner, and Y. H. Kuo, Artificial plasma cave in the low atitude ionosphere results from the radio occultation inversion of the FORMOSAT–3/COSMIC, *J. Geophys. Res.*, **115**, A07319, doi:10.1029/2009JA015079, 2010.

Marinov, P., I. Kutiev, and S. Watanabe, Empirical model of O+-H+ transition height based on topside sounder data, *Adv. Space Res.*, **34**, 2021–2025, 2004.

Rawer, K., D. Bilitza, and S. Ramakrishnan, Goals and status of international reference ionosphere, *Rev. Geophys.*, **16**, 177–181, 1978.

Sagawa, E., T. J. Immel, H. U. Frey, and S. B. Mende, Longitudinal structure of the equatorial anomaly in the nighttime ionosphere observed by IMAGE/FUV, *J. Geophys. Res.*, **110**, A11302, doi:10.1029/2004JA010848, 2005.

Y. Kakinami (e-mail: kakinami@mail.sci.hokudai.ac.jp), J.-Y. Liu, and L.-C. Tsai